

Investigating shock processes in bimodal powder compaction through modelling and experiment at the mesoscale

James G. Derrick^{a,*}, Michael E. Rutherford^b, David J. Chapman^{b,c}, Thomas M. Davison^a, Joao Piroto P. Duarte^c, Lukasz Farbaniec^c, Phil A. Bland^d, Daniel E. Eakins^{b,c}, Gareth S. Collins^a

^a*Department of Earth Science & Engineering, Imperial College London, London SW7 2BP, UK*

^b*Solid Mechanics and Materials Engineering, Department of Engineering Science, University of Oxford, Oxford OX1 3PJ, UK*

^c*Institute of Shock Physics, Blackett Laboratory, Imperial College London, London SW7 2BW, UK*

^d*Department of Applied Geology, Curtin University, GPO Box U1987, Perth, Western Australia 6845, Australia*

Abstract

Impact-driven compaction is a proposed mechanism for the lithification of primordial bimodal granular mixtures from which many meteorites derive. We present a numerical-experimental mesoscale study that investigates the fundamental processes in shock compaction of this heterogeneous matter, using analog materials. Experiments were performed at the European Synchrotron Radiation Facility generating real-time, *in-situ*, X-ray radiographs of the shock's passage in representative granular systems. Mesoscale simulations were performed using a shock physics code and set-ups that were geometrically identical to the experiments. We considered two scenarios: pure matrix, and matrix with a single chondrule. Good agreement was found between experiments and models in terms of shock position and post-shock compaction in the pure powder setup. When considering a single grain embedded in matrix we observed a spatial porosity anisotropy in its vicinity; the compaction was greater in the region immediately shockward of the grain, and less in its lee. We introduced the porosity vector, \mathbf{C} , which points in the direction of lowest compaction across a chondrule. This direction-dependent observation may present a new way to decode the magnitude, and direction, of a single shock wave experienced by a meteorite in the past.

*Corresponding author

Email address: james.derrick10@imperial.ac.uk (James G. Derrick)

Keywords: Mesoscale modelling, impact, shock compaction, heterogeneous, chondritic meteorites, X-ray radiography, granular media

1. Introduction

Recent studies have proposed that the meteorites we observe today were originally compacted and lithified from highly porous, bimodal mixtures in the early solar system through low ($0.5\text{--}3\text{ km s}^{-1}$) velocity planetesimal collisions (Bland et al., 2014; Davison et al., 2016; Forman et al., 2017). The mixtures consisted of mm-scale spherical solidified melt droplets (‘chondrules’) surrounded by a much finer (μm -scale grain) porous dust (‘matrix’). Such bimodal powder mixtures display an extremely heterogeneous response when subjected to shock compression and numerical studies have shown evidence of large variations in compaction and temperature ($> 500\text{K}$) on sub-chondrule length-scales (Bland et al., 2014). Previous investigations into these shock processes have been largely numerical (Bland et al., 2014; Davison et al., 2016) because of the inherent difficulty in studying real precursor meteoritic material, although some recent studies have bypassed this obstacle by using analog materials to represent chondrules and matrix (Beitz et al., 2013; Davison et al., 2017; Rutherford et al., 2017).

Here we present the results of an experimental-numerical approach to investigate the shock features and processes involved in bimodal compaction at the mesoscale. Our study builds on experimental protocols established in previous work (Rutherford et al., 2017). Mesoscale experiments were performed using *in-situ*, real-time, X-ray radiography of the shock compression process in analogous materials (Davison et al., 2017; Rutherford et al., 2017). Experiments measured heterogeneity in the shock compaction process in analog meteorite precursor materials. Equivalent simulations were performed using the 2D iSALE shock physics code (Collins et al., 2011; Wünnemann et al., 2006), which has been used extensively in the past to consider mesoscale shock compaction (Davison et al., 2016; Derrick et al., 2018; Güldemeister et al., 2013). This study begins by considering the interaction between a shock front and a single chondrule embedded in matrix (set up as in Figure 1).

Previous modelling studies (Bland et al., 2014; Davison et al., 2016) predict a dichotomy in the compaction around chondrules: higher densities ‘shockward’ (in the direction of the shock) and lower densities ‘leeward’ (in its lee) (Davison et al., 2016). Petrographic studies of meteorites post-compaction (Forman et al., 2017) have observed crystallographic preferred orientations (CPOs) in the matrix surrounding chondrules that are shock direction-dependent. This phenomenon may be consistent with the predicted dichotomy. A goal of the current work is to use experiments to close the loop, and link observed textures to model results. By considering an idealised scenario of a single chondrule within a matrix bed, we present evidence of the predicted spatial variation in compaction and its relationship with shock transit direction.

In addition, we devised a simple metric by which to measure the dichotomy: the porosity vector \mathbf{C} , which points in the radial direction of the mean porosity gradient of the annulus of matrix surrounding the chondrule. Initial analysis of simulations utilising a multi-chondrule bimodal mixture, with appropriate grain volume fractions (Bland et al., 2014), suggests that the porosity vector is not as strong in realistic scenarios, but points in the direction parallel to the bulk shock direction. This suggests that it could be a useful metric for decoding the shock stage of a meteorite.

2. Experimental method

Experiments were performed on Beamline ID19 at the European Synchrotron Radiation Facility (ESRF) using a dynamic X-ray radiography method (Rutherford et al., 2016, 2017). A 25 mm long, 12.5 mm diameter, polycarbonate sabot, with 2 mm copper flyer attached, was fired at targets using a 3 m single-stage gas gun and an impact velocity of $V_I \approx 600\text{ms}^{-1}$. An aluminium cell contained each powder sample, with a polycarbonate driver and PMMA window sealing each end (Figure 1). The matrix was represented by silica powder (grain size $\approx 7\mu\text{m}$, $\approx 70\%$ porosity, Sipernat 320-DS) and the chondrule by a borosilicate glass rod (1 mm diameter, 8 mm length); this was placed parallel to the shock, perpendicular to the axial direction, and end-on to the X-rays, to emulate a 2D simulation (Figures 1 & 6). The samples were pre-compacted before experiments (Sipernat naturally has $\phi \gtrsim 90\%$),

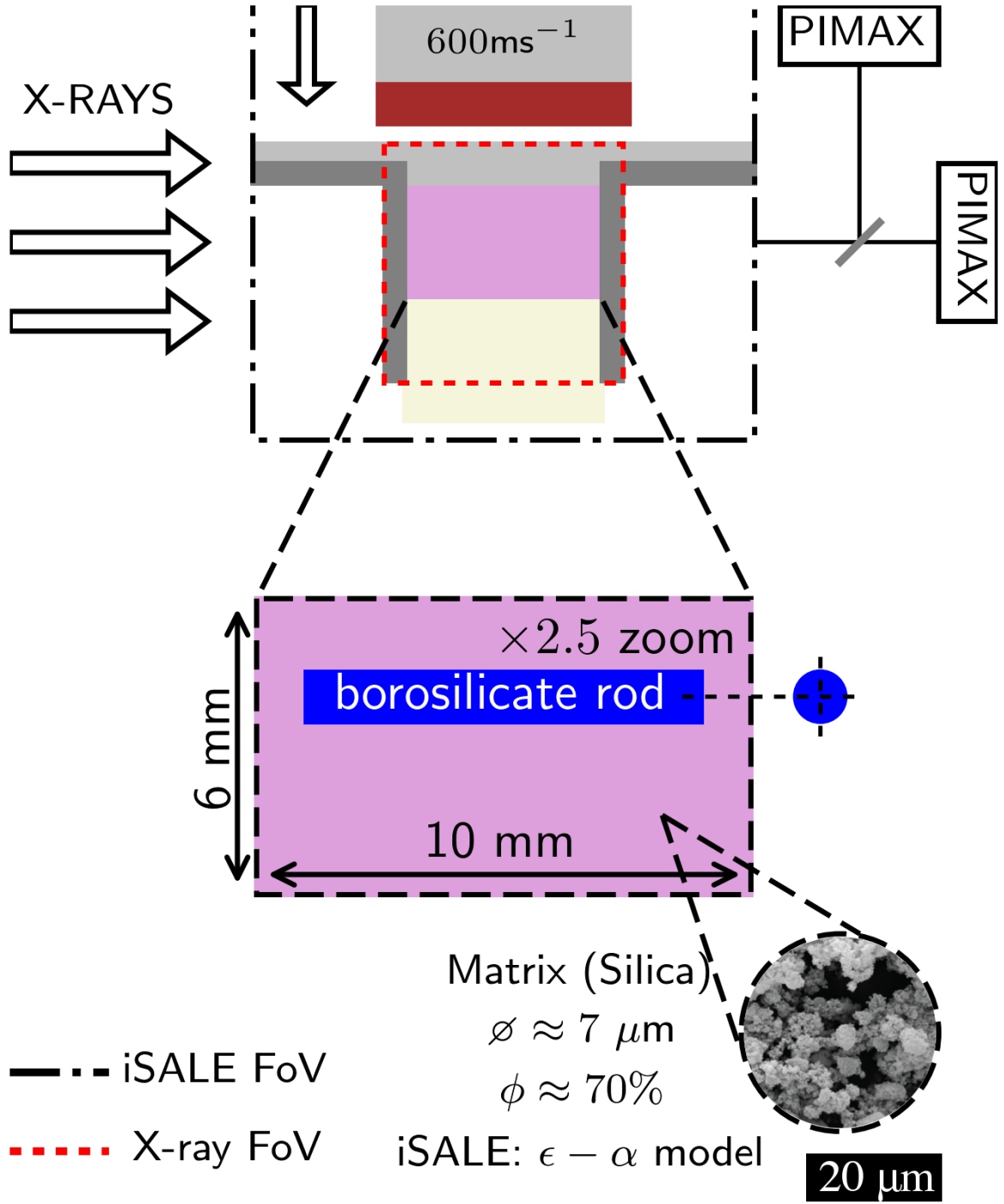


Figure 1: To-scale, cross-section of the setup used in both experiments and simulations, based on the experimental geometry used in previous work (Rutherford et al., 2017). Apart from the chondrule/rod and X-rays, the diagram is cylindrically symmetric. A flyer plate, backed by a sabot, impacted a powder cell containing either just the matrix material or the matrix material with a single chondrule analog.

however, this typically caused the rods to ‘misalign’ during preparation, which introduced an uncertainty on their location pre-shot (Figure 6; Frame 1).

Four radiographs were recorded per shot via a LYSO scintillator and two PI-MAX4:1024i cameras. The shock position was detected for every row of pixels in the shock propagation direction via difference imaging, which located the first pixel of intensity lower than that of the unshocked material within the limits of the noise. The material velocity behind the shock front was assumed to be equal to the velocity of the interface between the driver and powder, which was obtained from fitting a step-function across it, for each row of pixels, and dividing through by the shock transit time. The uncertainty in the position of the shock front was dominated by an assigned error of ± 2 pixels ($1 \text{ pixel} = 11.85\mu\text{m} \times 11.85\mu\text{m}$), equal to the measured line-spread function of the radiographic system. The uncertainty in the measured driver/powder interface position was taken as the width of the step-function fitted across it and was typically on the order of 10 pixels. Spatially-resolved, line integrated, mass densities were extracted from the radiographs through the use of a 2D numerical X-ray absorption model, which accounted for the full cell geometry, polychromatic X-ray spectrum and non-proportional scintillator response (Khodyuk and Dorenbos, 2012; Rutherford, 2017). For each converted porosity map quadrature analysis was performed to bound uncertainties in the calculated porosities. Of the sources of uncertainty considered (camera non-linearity, powder cell dimension changes during the shock, spatial filtering, scintillator thickness and non-proportionality response) the $\pm 1\%$ uncertainty in camera linearity was found to be dominant, leading to a typical uncertainty of $\pm 7\%$ in the calculated porosities including both systematic and random effects.

3. Mesoscale modelling

2D numerical simulations were performed with the shock physics code, iSALE (Davison et al., 2016; Wünnemann et al., 2006), and replicated the idealised experimental geometry in cylindrically symmetric setups (silica powder fill). 2D plane strain boundary conditions were used otherwise (silica powder fill with a single borosilicate glass rod). The simulations used the Mie-Grüneisen equation of state for all materials. The borosilicate glass and

polycarbonate were treated as elastic-perfectly plastic; the Copper and Aluminium used the Johnson-Cook strength model (Johnson and Cook, 1985); and the Sipernat used the Drucker-Prager model (Drucker and Prager, 1952). The Sipernat’s porosity was parameterised with the $\epsilon - \alpha$ porosity model (Collins et al., 2011; Wünnemann et al., 2006) with parameters tuned to Sipernat Hugoniot work by Chapman (Chapman, 2010) (Table 1). The final parameters predicted that 50% compaction (typical for this investigation) would be achieved at $\approx 0.2 - 0.4$ GPa and total compaction would require stresses beyond the range considered here ($\gtrsim 1$ GPa). Unreferenced parameters were chosen as sensible approximations and the strength model parameters were based on those presented in Wünnemann et al. (2016). Deng and Ko (1992) investigated the coefficient of friction between silicon and silicon compounds in a vacuum. While their work does not consider Sipernat directly, it does consider a variety of types of silicon, and silica in various combinations, suggesting that a friction coefficient of 0.5-0.7 is representative of this material. A value at the higher end of the scale was chosen to reflect that the experimental material had been pre-compacted before each experiment. This approach was necessary to generate a reasonable numerical model. This is because Sipernat is an unusual substance: it has a nominal porosity of 95% (Rutherford, 2017), for example, and its dynamic response is dominated by its granular nature; see work by Borg *et al.* for details (Borg et al., 2006). Our parameters, however, are otherwise consistent with existing work (Lyzenga et al., 1983; Wackerle, 1962) and we show that the resulting Hugoniot is in good comparative agreement with experimental data (Figure 2).

The equation of state (EoS) parameters were taken from a variety of sources in the literature (Table 1) and analytical, strengthless, Hugoniots in shock-particle velocity and pressure-density space were calculated from these. These Hugoniots were checked against shock-particle velocity and stress-density data for agreement. To accurately assess the parameters chosen for the silica a suite of simple 1D planar impact simulations (with porosity $\phi = 65\%$) were conducted in order to extract a more physically realistic shock-particle velocity/stress-density Hugoniot. This enabled a comparison of the iSALE Hugoniot, where the strength of the silica was also factored in, with an experimental Hugoniot (also $\phi = 65\%$).

Table 1: Full details of all parameters used for Sipernat in iSALE. *The ‘Limiting strength’ is the strength of the material at infinite pressure.

EoS Parameters

Solid density [gcm^{-3}]	2.203 (Wackerle, 1962)
Sound speed, c_0 [ms^{-1}]	1400 (Borg et al., 2006)
Grüneisen gamma, Γ	0.036 (Wackerle, 1962)
$U_s - u_p$ constant, S	1.1 (Borg et al., 2006)
Specific heat capacity [$\text{JK}^{-1}\text{kg}^{-1}$]	740

Strength Parameters

Cohesion [kPa]	10
Coefficient of internal friction	0.7 (Deng and Ko, 1992)
Limiting strength* [MPa]	100
Poisson ratio	0.3

$\epsilon - \alpha$ Parameters

Elastic threshold, ϵ_0	0
Transition distension, α_x	1.29
Exponential coefficient, κ	0.8
Sound speed ratio, χ	0.33

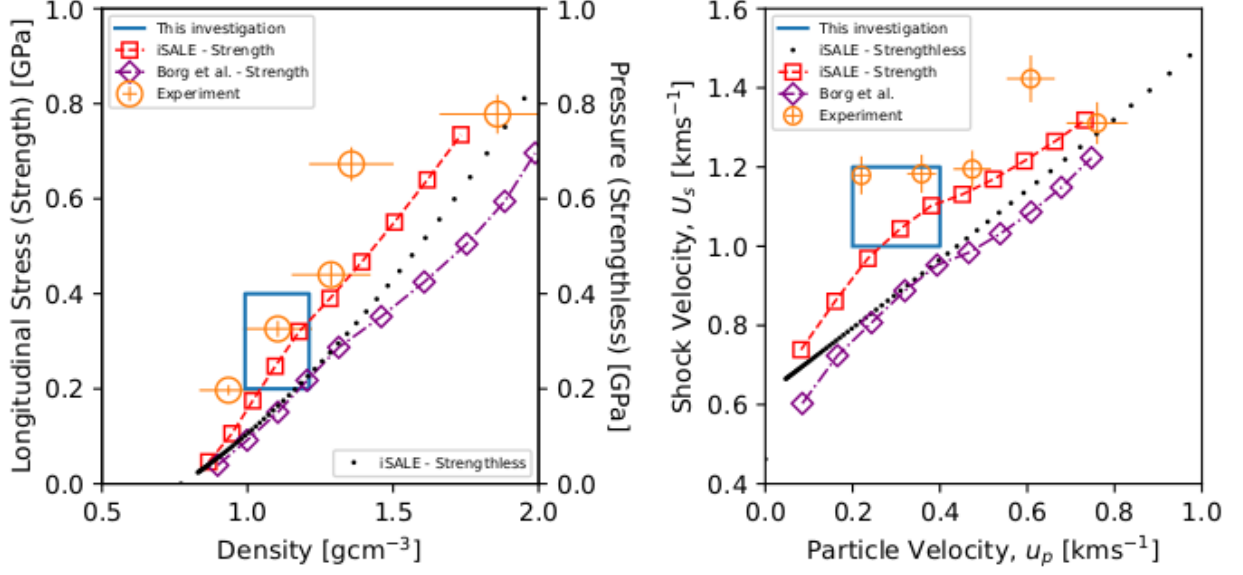


Figure 2: Hugoniot taken from iSALE using fitted $\epsilon - \alpha$ parameters compared with experimental Siper-nat Hugoniot data (Chapman, 2010). Hugoniot using EoS parameters taken from Borg *et al.* (Borg et al., 2006) used for comparison. The typical stresses, densities and velocities observed in this investigation are represented as blue regions on each plot. All Hugoniot in these plots use an initial density of 0.77 gcm^{-3} ($\phi \approx 65\%$).

The iSALE results appear to underestimate the experimental data slightly in shock-particle velocity space but are in good agreement in pressure-density space (Figure 2). An explicitly extracted Hugoniot, created from other published EoS parameters for the same material ($\phi = 65\%$), is included for comparison (Borg et al., 2006). These parameters have been used in previous investigations that involved full mixtures of chondrules and matrix, which showed good agreement between the models and experiments (Davison et al., 2017).

4. Results and Discussion

4.1. Pure Matrix Response

Four radiographs were recorded in each experiment. To ensure consistency of shock transit timing between experiment and simulations, the first radiograph frame of the experiment was matched with the closest equivalent simulation frame. This frame was taken as the reference time, T_0 and subsequent times were measured relative to it. The three comparative

radiograph frames are consistent with the numerical model results, although the experiments display significant bowing of the shock at the edges of the sample. Additional cylindrically symmetric simulations were performed to investigate the cause of the bowing. These simulations suggest that the bowing is caused by a combination of two factors in the experiments: existing porosity gradients in the powder sample and uncertainties on the drivers' diameter.

Production of the powder samples required that they be pre-compacted to the desired densities; uniform pressure was applied across the cell during crushing, however, some density gradients probably still formed because of the finite size of the cell. Powder near the cell walls, for example, would have experienced greater pressure because it was restricted by the cell walls as well as the applied pressure (the powder was crushed axially along the cell). Simulations were designed to examine the effects this would have had on the powder's response. As a first approximation the porosity was assumed to vary by approximately its uncertainty in each pixel ($\sim 10\%$). The density was greatest at the cell wall, becoming more porous toward the centre. Discrete, vertical, bands of material were used in the simulations to simulate the varying porosity. The results of these simulations demonstrated that the introduction of porosity gradients in the powder bed was sufficient to cause bowing of the shock front at late times. They did not, however, display the same bowing at early times. Additional simulations suggested that the shock front was probably bowed before it entered the sample and that this was caused by uncertainties on the drivers' diameter.

The powder sample was contained within a cylinder of aluminium that was plugged by the driver at one end, and a PMMA window at the other. Additional simulations suggested that if there was some non-zero clearance between the driver and the aluminium cell wall then the shock would release laterally before entering the powder bed. This lateral release would be sufficient to bow the shock near the cell wall before it entered the powder. The uncertainty (machining tolerance) on the driver's diameter was ~ 0.1 mm, which the additional simulations suggested was sufficient to bow the edges of the shock at early times.

By combining the effects of introducing a 'gap' between the driver's transverse face with the cell wall, and the probable porosity gradients in the powder, it is possible to qualita-

tively reproduce the bowing seen in the experiments. In addition to these effects, there is another feature that exacerbates the effects seen: off-axis tilt of the impact. In Figure 3 the driver/powder interface is distinctly non-perpendicular to the direction of shock propagation, whilst the cell walls appear to remain approximately parallel to it. This suggests that the flyer struck the sample at an angle, which in turn drove a non-planar shock through the apparatus. It is extremely challenging to deduce the precise angle of impact from the radiographs because they are 2D projections of a 3D event and can not record information about the extent to which impact was tilted into/out of the page. In addition, this effect is likely to have affected the bowing that was observed, by generating an asymmetric shock front.

To reduce the effects of the bowing and tilt when comparing the results of the simulations with the experiments all subsequent analyses considered a centred, $750\text{ }\mu\text{m}$ wide, region of the bed. This was equivalent to 100 mean grain diameters, where the shock front is approximately planar in both experiments and models (dubbed the ‘on-axis region’).

The shock position was measured explicitly by tracking its average on-axis position, relative to the static driver/powder interface, at each time (Figure 4). The shock positions in the models and experiments are difficult to compare because of the various factors affecting the experiment, tilt in particular. Reducing analysis to only the on-axis region ensures that the shock can be approximated as planar in both simulations and experiments. When considering the shock positions, both experiments and simulations exhibit a slight reduction in gradient as the shock progresses. The models appear to lead the experiment, as seen in Figure 3. The agreement between positions suggests that the the simulation is modelling the powder’s compaction appropriately.

The use of radiography to image the shock propagation allows for the extraction of spatial density, and hence porosity, maps. These can be easily compared with the simulation results. The relative compaction behind the shock, (in the on-axis region) for both the experiment and simulation is presented in Figure 5. To compare equivalent longitudinal positions between the simulations and the experiments, longitudinal porosity lineouts were plotted in the driver

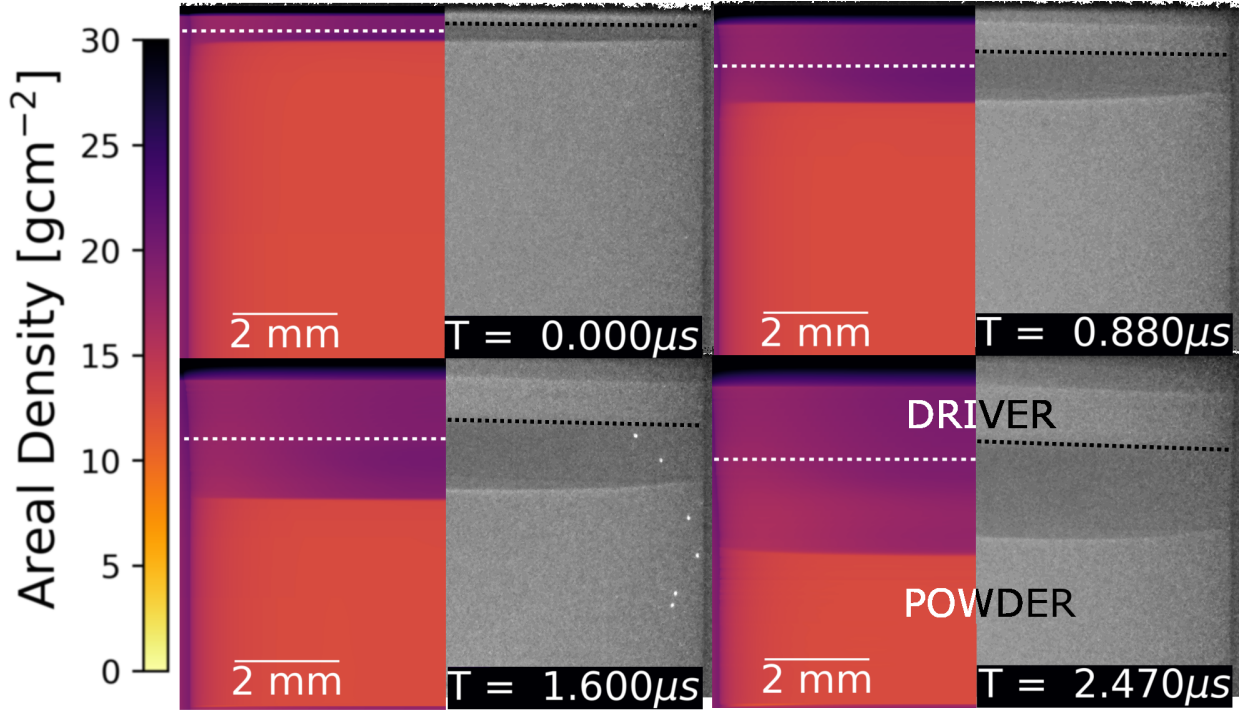


Figure 3: Direct radiograph/model comparison. Models are on the left and radiographs on the right; the times are calibrated against frame 1 which is T_0 . The white/black dashed lines represent the driver/powder interface in the simulations and radiographs respectively. Model data is projected into areal density to facilitate comparison with the radiographs. Impact direction is down the page and none of the shocked powder has released in any frame.

frame. There appears to be good agreement between the experiments and models (Figure 5). The simulation data are within experimental fluctuations in all frames, which are $\pm \sim 7\%$ porosity. Additionally, the longitudinal shape of compaction behind the shock is consistent between models and experiments; there is a small gradient in porosity that decreases further behind the shock and then undergoes a large rise at the driver interface. This agreement in post-shock compaction is clear evidence that the simulations are correctly modelling the experimental shock compaction. It suggests that the mismatch in shock-front position stems from differences in how the shock front is found between the models and experiments, which were not the same because of the differences in output (radiographs vs density maps). These results provide additional evidence that iSALE accurately reproduces the shock response of the matrix.

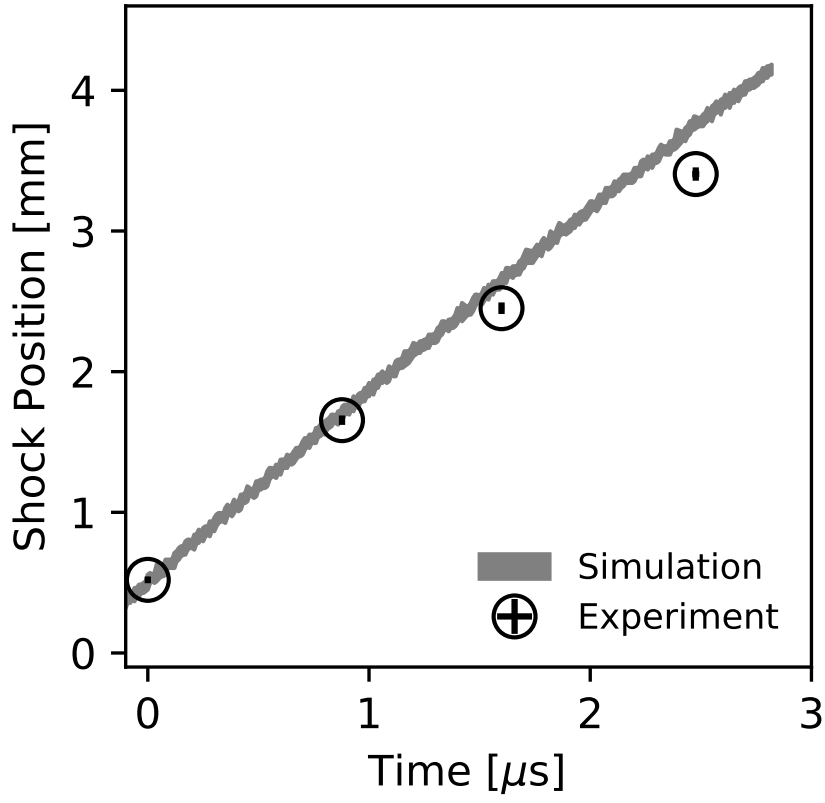


Figure 4: Evolution of shock position with time, in experiments and simulations. Simulation band represents the full range of positions at that time. Experimental error bars are small at the scale of this plot, and are shown by the black bars inside the open circle symbols.

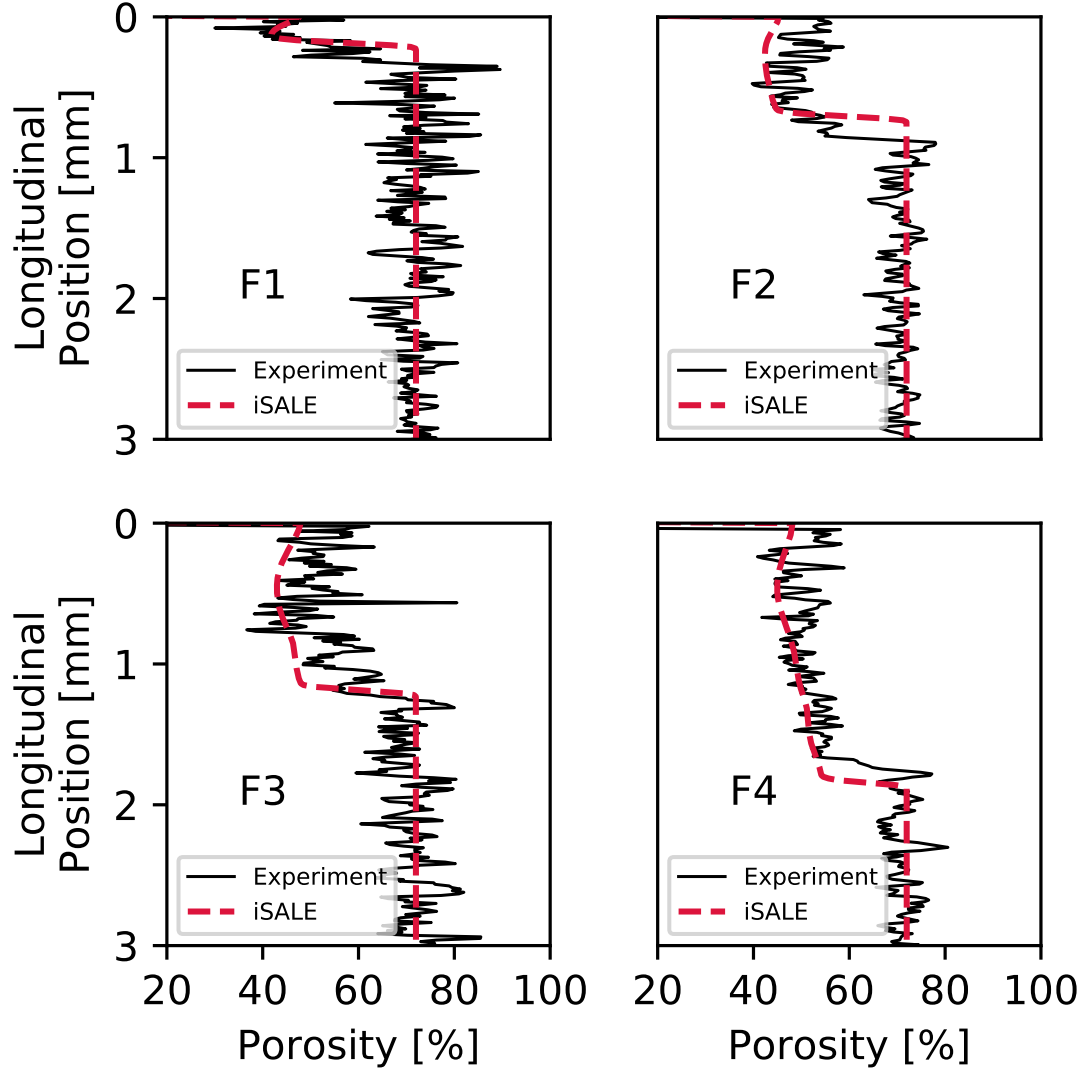


Figure 5: Longitudinal porosity line-outs of the on-axis porosity at each time for both experiments and simulations. Positions are relative to the driver/powder interface in each frame, which corresponds to the origin in each plot.

4.2. Matrix/Chondrule Interaction

The results of matrix compaction with a single, embedded chondrule are similarly consistent between experiments and models (Figure 6). The same general pattern of compaction, as observed in the pure matrix, is present. Once the shock has passed the chondrule, however, a dichotomy in compaction appears in the matrix around it. This anisotropy appears to depend on the direction of shock passage (Figure 6). The material ahead of the chondrule (in the direction of the shock’s propagation; ‘leeward’) is more porous compared to adjacent matrix; the chondrule appears to have ‘shielded’ some of the matrix in its lee from compaction. Conversely, the matrix behind the chondrule (pointing toward the driver; ‘shockward’) appears to be less porous than adjacent matter. Some of the shock energy has been reflected at the first interface between chondrule and matrix and the matrix between the driver and chondrule has been subsequently re-shocked to a higher density (Figure 7, F3 & F4).

We quantitatively compare the two compaction features by taking lateral lines of porosity at identical longitudinal positions in both experiment and simulation, 250 μm leeward and 125 μm shockward of the chondrule (Figure 7). Experimental uncertainties come from noise in the radiographs and model uncertainties come from uncertainty in the exact rod position ($\pm 25 \mu\text{m}$) owing to rod misalignment during sample preparation. Both the experiment and model show agreement in the transverse size of the chondrule’s area-of-effect (region of matrix affected by the addition of the chondrule), which is, $\approx 1.5 \text{ mm}$ wide (~ 1.5 chondrule diameters). Leeward, there is good agreement in porosity, although the ‘shielded’ region is difficult to discern in the experiments because the porosity difference is on the order of its uncertainty. Shockward, there is greater compaction in the models than in the experiment. It is likely that this discrepancy is primarily caused by two factors. The first is that the experiments are not perfectly 2D; the rod is 8 mm long, leaving $\approx 1 \text{ mm}$ of matrix either side that is unaffected by the rod. This will not be compacted as much as the material between the rod and driver, but will be compacted more than the material in the rod’s lee. This will lead to a higher line-integrated porosity than in the models shockward of the rod and a lower line-integrated porosity in the rod’s lee. This effect will reduce the amplitude of the

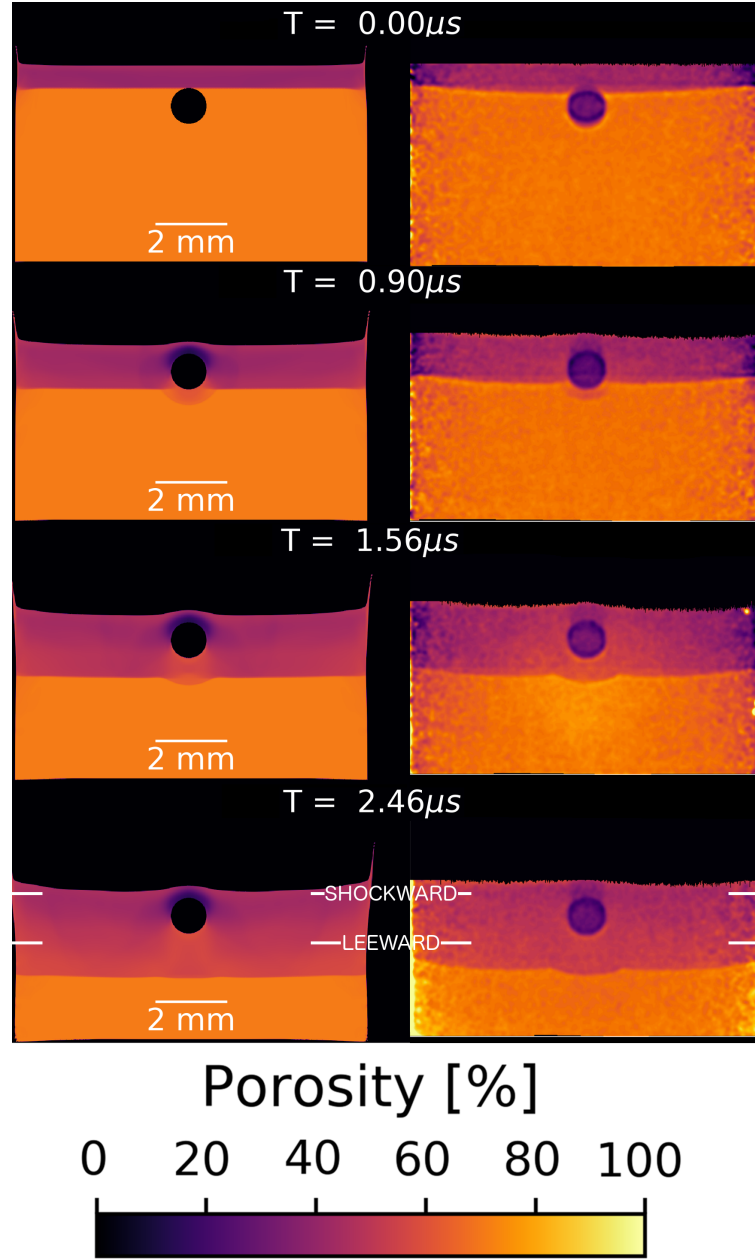


Figure 6: Time series of modeled (left) and experimental (right) porosity maps recorded during the shock-compression of matrix and chondrule samples. Both series use the same scale, impact direction is down the page, and the porosity line-out positions are indicated in white on the last frame.

dichotomy in the experiments. The second factor is that the model used for the Sipernat was developed against a limited Hugoniot of five points that did not focus on the region of interest for this investigation. Whilst the model has generally shown good agreement with the experiments broadly, it is possible that a more nuanced model would produce closer agreement.

4.3. Porosity Vector

The joint numerical-experimental evidence of anisotropic compaction around a single grain presents a potential method of decoding the magnitude and direction of the shock that a chondrule experienced. However, whilst its existence is clear in an idealised scenario, the feature's presence in a more realistic mixture is less certain. To investigate the extent of the dichotomy's presence in more realistic scenarios the compaction surrounding chondrules in a full mixture was considered. If the dichotomy in compaction around grains is present in a more realistic simulation it is likely that each grain will experience different magnitudes, and the direction of the compaction gradients may not align. The 'porosity vector' (\mathbf{C}) was devised as a simple metric to quantify the magnitude, and direction, of the anisotropic compaction around a chondrule.

\mathbf{C} is a polar vector (with the chondrule centre as its centre) that points along the mean porosity gradient across a chondrule (Figure 8). The porosity vector's angle is measured with respect to the direction of impact/intended shock direction: a value of 0° indicates the porosity vector points in the same direction as the shock's propagation, whereas a value of $\pm 180^\circ$ indicates the porosity vector points where the shock has been. Positive and negative angles indicate directions left, and right, of the diagrams respectively and this choice is arbitrary. The porosity vector is calculated using the matrix within its area-of-effect, specifically an annulus that extends from the chondrule's rim by $\frac{1}{4}$ the chondrule diameter ($250\mu\text{m}$). This annulus of matrix is split into 20 'wedges' (annulus sectors), with equal arc lengths. The average porosity in each wedge was found. The relative difference in porosity across the grain was found by taking the difference in porosity between opposite wedges. This produced 10 equi-spaced polar vectors that pass through the chondrule's centre. The weighted

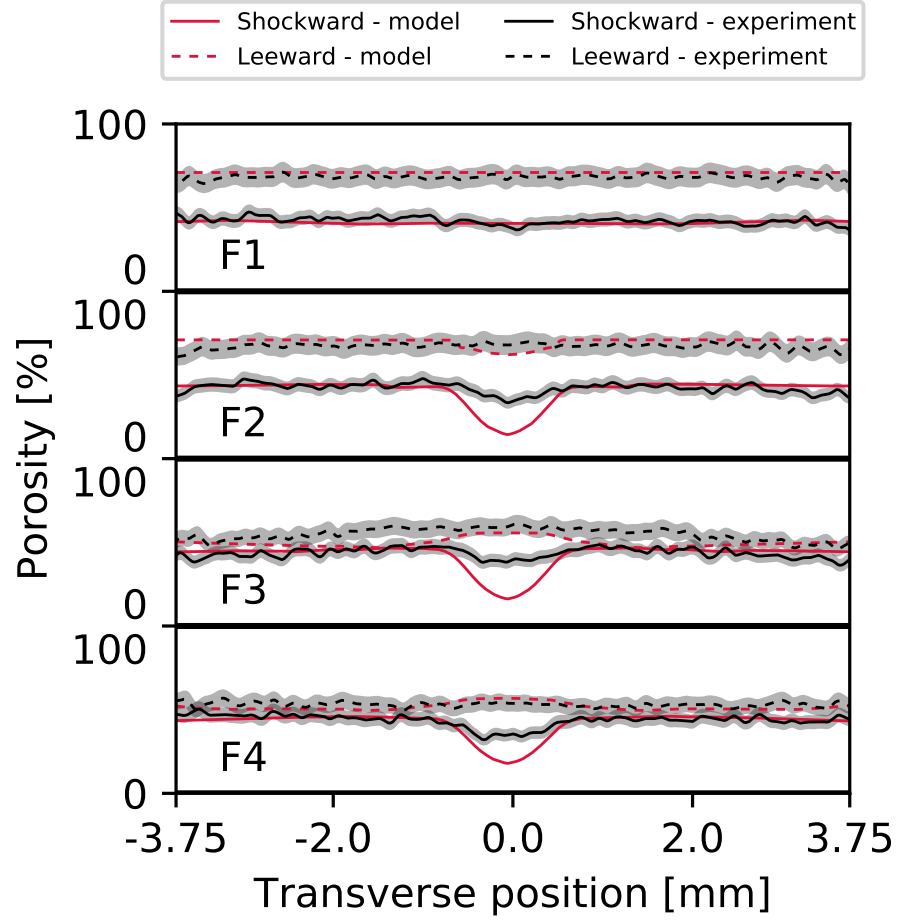


Figure 7: Lines of porosity taken at the same longitudinal positions ($250 \mu\text{m}$ ‘ahead’—leeward— and $125 \mu\text{m}$ ‘behind’—shockward— of the chondrule, marked in white in Figure 6) in each frame (F1-4). In frames 1 & 2 the shock has not reached the leeward position and the line indicates the porosity of the unshocked material.

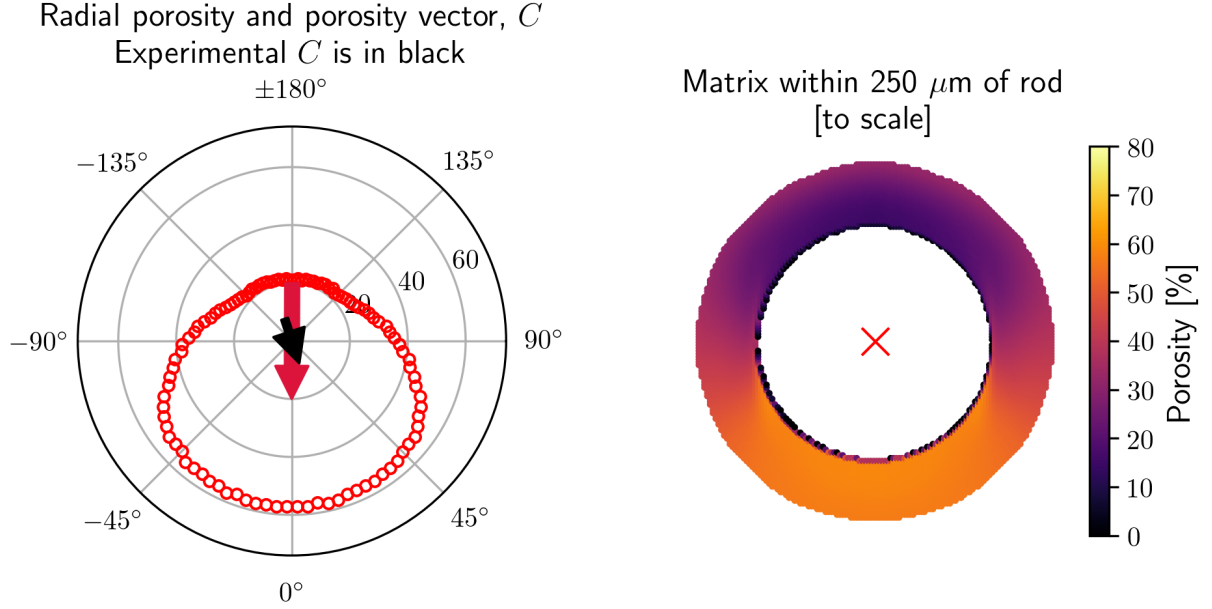


Figure 8: (Left) Numerical and experimental porosity vectors of the chondrule. The red arrow represents the numerical porosity vector, C with a length of $2|C|$ and was calculated from 20 equi-spaced ‘wedges’ of matrix surrounding the single chondrule. The red circles show the porosity surrounding the chondrule (split into 100 wedges for visualisation purposes). The black arrow represents the equivalent experimental value of C . (Right) $\frac{1}{4}$ chondrule diameter wide ($250\ \mu\text{m}$) annulus of matrix around the chondrule in Figure 7. This was split into 100 wedges/annulus sectors (with the red cross as each wedge’s centre) to produce the left-hand image. Both plots are presented in the same orientation as previous figures (impact travelling down the page).

average of these 10 vectors (magnitude and angle separately) is the resulting porosity vector. In the single chondrule scenario the porosity vector is parallel to the shock direction ($\theta \approx 0^\circ$) and has a magnitude of $\approx 20\%$ (Figure 8). This means that on average there is a positive porosity gradient, and that there is on average a difference of 20% porosity for an angle of $\theta \approx 0^\circ$. The experimental \mathbf{C} is 5-10° away from perfectly vertical, with an estimated uncertainty of $\sim \pm 2.5^\circ$ (weighted standard deviation of the mean angle) on its direction, which puts it in approximate directional agreement with the simulations. The uncertainty on the simulation's porosity vector was $\sim \pm 4\%$ on the magnitude and $\sim \pm 1.3^\circ$ on the direction. The simulation analysis suggests that the direction of the porosity vector will be the same as the direction of the shock wave propagation. The experimental porosity vector's small angle to the vertical suggests that the experimental shock wave did not travel exactly vertically down the page. This is consistent with the suggestion that the tilt caused the shock to propagate at an angle to the intended direction, as well as 0° being outside of the experiment \mathbf{C} directional uncertainty. The experimental porosity vector direction is in closer agreement to the estimated amount of tilt ($\sim 5^\circ$) than it is to the simulation's porosity vector direction. The magnitude of the experiment's \mathbf{C} , however, is significantly less than the model's. This is consistent with the experimental transverse porosity lineouts, which showed the max difference between porosities across the chondrule in the experiment was much less than the simulation.

\mathbf{C} is a useful metric to describe the relative compaction across a chondrule. It is the weighted average of compaction gradients that cross the centre of the chondrule and so it will be insensitive to some compaction geometries. For example, in real multi-chondrule systems a common feature is a chondrule that is 'squeezed' such that it has compressed matrix on opposite sides, which is typically caused by nearby chondrules. This identically uncompressed matrix on the two sides perpendicular to the first pair will always return $\mathbf{C} = 0$. Despite the presence of a dichotomy in compaction, the porosity vector will return the same result as if there had been no compaction at all. \mathbf{C} is insensitive to compaction dichotomies with more than a single line of symmetry, which makes it an ideal metric for

use in multi-chondrule systems because incidents of symmetric compaction (or close to) are common as chondrules are forced together.

To examine how the porosity vector changes in a more realistic, non-idealised, system a simulation was performed consisting of many chondrules using a set-up that was representative of the materials present in precursor meteorite matter. The mixture fractions, and sizes, for the ‘realistic’ simulation were taken from previous work (30 %vol chondrules; 70 %vol matrix; matrix porosity $\approx 70\%$, and chondrule diameter 0.5 mm). These numbers are representative estimates of pre-compaction material properties based on ‘decompacted’ observations of the Allende meteorite (Bland et al., 2014; Davison et al., 2017; Rutherford et al., 2017). The simulations were simple 2D planar columns. The chondrules were randomly distributed within the particle bed as would be expected in a realistic arrangement (Figure 9). The general level of compaction is broadly comparable to the ranges seen in the single chondrule scenario, given the similar V_I and ϕ , but it is not visually obvious if there are porosity dichotomies around individual chondrules. Visual observations are particularly difficult in regions where chondrules have come into contact, or close proximity, with each other because of the additional regions of compaction this creates.

Chondrules that have come into contact with each other were ignored because they had become ‘welded’ together, which hindered the algorithm used to calculate \mathbf{C} . Additionally, chondrules that were partially within the domain were ignored because they did not have a clear centre, or annulus of surrounding matter with which to calculate \mathbf{C} . The compaction shapes have fewer axes of symmetry, if any, than in the idealised case, but regions of less compaction are still present leeward of the chondrules. All the chondrules that \mathbf{C} was calculated for (approximately half of the grains in the bed) possessed a downward pointing vector (Figure 10). Their directions appear to be normally distributed about 0° , the direction of shock propagation. The magnitudes of \mathbf{C} are approximately half that of the idealised case, and more consistent with the experimental value of \mathbf{C} for the single chondrule case, despite comparable impact velocities $\sim 600\text{ms}^{-1}$ and less lateral release. It is unlikely that the matrix grain size affected the porosity vector because each pixel (pre-shock and in the vicinity of

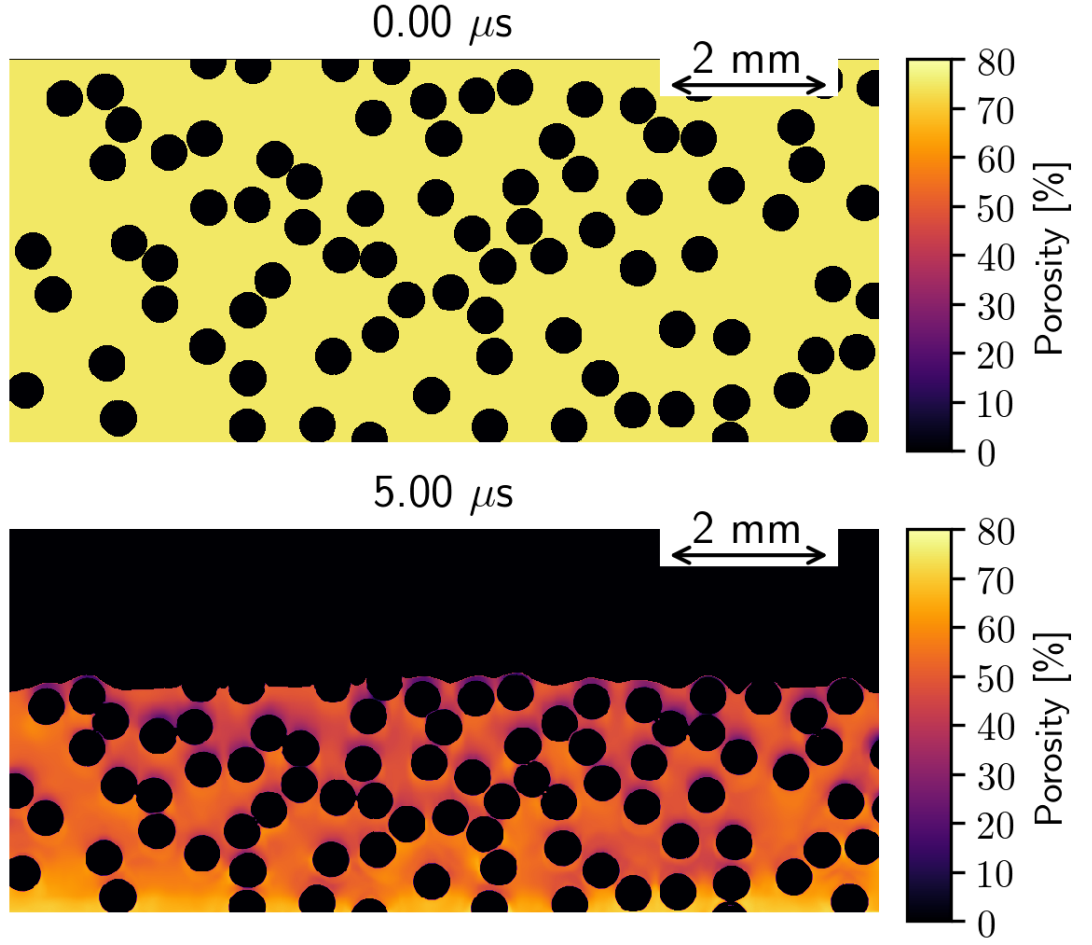


Figure 9: Simple planar impact simulation, using a full chondrule/matrix mixture (30 %.vol chondrules; 70 %.vol matrix), matrix porosity $\approx 70\%$, and chondrule diameter 0.5 mm. The particle bed is 10 mm \times 4 mm and uses an impact velocity of $\approx 600\text{ms}^{-1}$. The scale, and features, are deliberately comparable with those already shown. The chondrule material was soda-lime glass as opposed to borosilicate glass, but still used a Mie-Grüneisen EoS and Von Mises strength model. This choice was made to match existing work more closely (Rutherford et al., 2017).

the chondrule) contains 1500-2000 grains. A probable cause is that the proximity of the chondrules may cause one chondrule's shockward region to interfere with another's lee. This overlap would reduce the difference in compaction across some chondrules and hence reduce the magnitude of \mathbf{C} .

The existence of this porosity vector has significant implications for the shock categorisation of meteorites. It could be used to provide information about the direction a meteorite was stuck in the past. NWA5000, for example is a meteorite that exhibits large dark regions (like shadows) on one side of its large embedded grains. These 'shadows' additionally have a preferred orientation across the meteorite. This feature could be a symptom of shock compaction and agreement with the porosity vector would be strong evidence for this. The porosity vector could also potentially reveal subtleties about a meteorite's chondrule distribution. If the chondrules of a meteorite possessed a general preference in orientation for a certain direction (chondrules do not typically retain their initial spherical shape over time (Forman et al., 2017; Nakamura et al., 1992)), as they do in the Leoville meteorite, for example, directional agreement with the porosity vector could provide evidence that the orientation preference is related to shock compression. Porosity maps of meteorites do not currently exist, however, there has been significant work examining similar features (Forman et al., 2017). It has been found, for example that the matrix in the Allende meteorite possesses crystallographic preferred orientations that tend to point in a preferred direction, which is attributed to shock direction (Forman et al., 2017). An agreement between the crystallographic preferred orientation and porosity vector directions in a meteorite would be good evidence that both are symptoms of the same phenomenon. Subsequent investigations could also consider how the magnitude of \mathbf{C} relates to the strength of the crystallographic preferred orientations, which would calibrate the magnitude of \mathbf{C} against known shock conditions.

5. Conclusions

We present a joint experimental-numerical investigation of mesoscale features of shock compaction of analog meteorite precursor mixtures of fine-grained matrix dust and larger, spherical, solid chondrules. The experimental and numerical, on-axis shock positions agreed

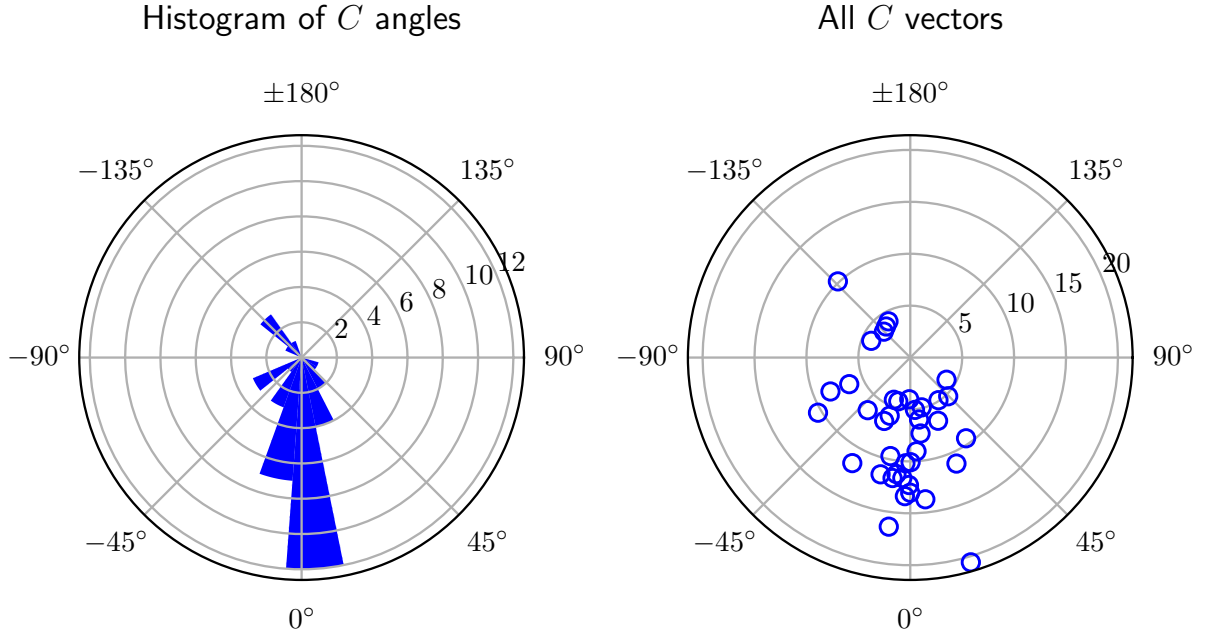


Figure 10: Statistics of the porosity vectors of all valid grains from Figure 9. (Left) histogram of C angles; they appear to be normally distributed about 0° . (Right) All the extracted porosity vectors plotted in polar space. Grains that were partially within the domain were ignored, as were grains in contact with another because the compaction surrounding these would be dominated by collision effects.

to within 10% at all times and the longitudinal variation in post-shock compaction was in close agreement. The addition of a single chondrule embedded in the matrix results produced spatial variations in matrix compaction around the chondrule that are consistent between experiments and numerical simulations and relate to the shock direction. When the shock wave encounters the isolated chondrule some energy is reflected resulting in less energy transmitted into the chondrule. As a result, the chondrule ‘shields’ material as the shock passes, reducing compaction in its lee. At the same time, the reflected wave energy reshocks matrix material on the shockward side resulting in enhanced compaction on that side. Quantifying matrix compaction around chondrules, therefore provides a potential method of decoding shock direction and magnitude from existing meteoritic evidence (Forman et al., 2017).

By considering the radial distribution of porosity around chondrules we devised a simple metric to measure the direction and magnitude of the relative compaction across the particle: the porosity vector, \mathbf{C} . An additional simulation, based on previous work (Davison et al., 2017; Rutherford et al., 2017), suggested that the porosity vector is typically non-zero in multi-chondrule set-ups, albeit with a reduced magnitude than what was observed in the single-chondrule case. Finally, we observed that the direction of the porosity vector varied between chondrules in the full mixture, but rarely pointed in the direction from which the shock wave came (shockward). Future work will explore the influence of non-spherical grain shape, as well as particle size, on this shock direction indicator. In addition, future work will investigate how the porosity vector depends on the strength of the shock wave.

In addition to investigating mesoscale compaction mechanics heterogeneous compaction studies of the kind presented could also be used to provide further insight into recent microscale observations, such as how to discourage catastrophic crack propagation in highly-heterogeneous concretes (Parab et al., 2016), the effects of other mesostructures on shock reponse (Derrick et al., 2018) or shock wave perturbation decay in granular materials (Vogler, 2015).

The work discussed here presents a potential method of decoding the direction and shock magnitude that meteorites experienced in their formation. Further work is necessary, how-

ever, in order to establish links with existing meteorite phenomena, such as preferred crystallographic orientations (Forman et al., 2017). This could lead to calibrating of the effects of C against known meteorite samples and the development of a new meteorite shock stage classification technique.

Acknowledgments

JGD gratefully acknowledges support from EPSRC EP/M506345/1. We thank the iSALE developers (www.isale-code.de) and the ESRF for their providing of the facilities necessary to perform the experimental work. TMD and GSC were supported by STFC grant ST/N000803/1. MER, DJC and DEE thank EPSRC and AWE for their support. JPPD acknowledges support from EPSRC EP/K028707/1 and LF from EPSRC EP/K034332/1.

Beitz, E., Güttler, C., Nakamura, A. M., Tsuchiyama, A., Blum, J., 2013. Experiments on the consolidation of chondrites and the formation of dense rims around chondrules. *Icarus* 225 (1), 558.

Bland, P. A., Collins, G. S., Davison, T. M., Abreu, N. M., Ciesla, F. J., Muxworthy, A. R., Moore, J., 2014. Pressure-temperature evolution of primordial solar system solids during impact-induced compaction. *Nature Communications* 5.

Borg, J. P., Cogar, J. R., Lloyd, A., Ward, A., Chapman, D., Tsembelis, K., Proud, W. G., 2006. Computational simulations of the dynamic compaction of porous media. *International Journal of Impact Engineering* 33 (112), 109–118.

Chapman, D. J., 2010. Shock-compression of porous materials and diagnostic development. Ph.D. thesis, University of Cambridge.

Collins, G. S., Melosh, H. J., Wünnemann, K., 2011. Improvements to the $\epsilon - \alpha$; porous compaction model for simulating impacts into high-porosity solar system objects. *Int. J. Impact Eng.* 38 (6), 434.

- Davison, T. M., Collins, G. S., Bland, P. A., 2016. Mesoscale modeling of impact compaction of primitive solar system solids. *The Astrophysical Journal* 821 (1), 1.
- Davison, T. M., Derrick, J. G., Collins, G. S., Bland, P. A., Rutherford, M. E., Chapman, D. J., Eakins, D. E., 2017. Impact-induced compaction of primitive solar system solids: The need for mesoscale modelling and experiments. *Procedia Engineering* 204, 405.
- Deng, K., Ko, W. H., 1992. A study of static friction between silicon and silicon compounds. *Journal of Micromechanics and Microengineering* 2 (1), 14.
URL <http://stacks.iop.org/0960-1317/2/i=1/a=004>
- Derrick, J. G., LaJeunesse, J. W., Davison, T. M., Borg, J. P., Collins, G., 2018. Mesoscale simulations of shock compaction of a granular ceramic: effects of mesostructure and mixed-cell strength treatment. *Modelling and Simulation in Materials Science and Engineering*.
- Drucker, D. C., Prager, W., 1952. Soil mechanics and plastic analysis or limit design. *Quarterly of Applied Mathematics* 10, 157.
- Forman, L., Bland, P., Timms, N., Daly, L., Benedix, G., Trimby, P., Collins, G., Davison, T., 2017. Defining the mechanism for compaction of the CV chondrite parent body. *Geology* 45 (6), 559.
- Güldemeister, N., Wünnemann, K., Durr, N., Hiermaier, S., 2013. Propagation of impact-induced shock waves in porous sandstone using mesoscale modeling. *Meteoritics & Planetary Science* 48 (1), 115–133.
- Johnson, G. R., Cook, W. H., 1985. Fracture characteristics of three metals subjected to various strains, strain rates, temperatures and pressures. *Engineering Fracture Mechanics* 21 (1), 31.
- Khodyuk, I. V., Dorenbos, P., 2012. Trends and Patterns of Scintillator Nonproportionality. *IEEE Trans. Nucl. Sci.* 59 (6), 3320–3331.

- Lyzenga, G. A., Ahrens, T. J., Mitchell, A. C., 1983. Shock temperatures of SiO₂ and their geophysical implications. *Journal of Geophysical Research: Solid Earth* 88 (B3), 2431–2444.
- Nakamura, T., Tomeoka, K., Takeda, H., 1992. Shock effects of the leoville CV carbonaceous chondrite: a transmission electron microscope study. *Earth and Planetary Science Letters* 114 (1), 159 – 170.
- Parab, N. D., Guo, Z., Hudspeth, M., Claus, B., Lim, B. H., Sun, T., Xiao, X., Fezzaa, K., Chen, W. W., 2016. In situ observation of fracture processes in high-strength concretes and limestone using high-speed x-ray phase-contrast imaging. *Philosophical Transactions of the Royal Society A: Mathematical, Physical and Engineering Sciences* 375 (2085), 20160178.
- Rutherford, M. E., 2017. Studies of shock compression at the mesoscale with synchrotron x-ray phase-contrast radiography. Ph.D. thesis, Imperial College London.
- Rutherford, M. E., Chapman, D. J., Derrick, J. G., Patten, J. R. W., Bland, P. A., Rack, A., Collins, G. S., Eakins, D. E., 2017. Probing the early stages of shock-induced chondritic meteorite formation at the mesoscale. *Sci. Rep.*, 1.
- Rutherford, M. E., Chapman, D. J., White, T. G., Drakopoulos, M., Rack, A., Eakins, D. E., 2016. Evaluating scintillator performance in time-resolved hard x-ray studies at synchrotron light sources. *J. Synchrotron Rad.*, 1.
- Vogler, T. J., 2015. Shock Wave Perturbation Decay in Granular Materials. *Journal of Dynamic Behavior of Materials* (August).
- Wackerle, J., 1962. Shock-Wave Compression of Quartz. *Journal of Applied Physics* 33 (3), 922.
- Wünnemann, K., Collins, G. S., Melosh, H. J., 2006. A strain-based porosity model for use in hydrocode simulations of impacts and implications for transient crater growth in porous targets. *Icarus* 180 (2), 514.

Wünnemann, K., Zhu, M.-H., Stffler, D., 2016. Impacts into quartz sand: Crater formation, shock metamorphism, and ejecta distribution in laboratory experiments and numerical models. *Meteoritics & Planetary Science* 51 (10), 1762–1794.
URL <https://onlinelibrary.wiley.com/doi/abs/10.1111/maps.12710>